


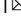



## Gapless fermionic excitation in the antiferromagnetic state of ytterbium zigzag chain

Fumiya Hori<sup>1</sup><sup>✉</sup>, Katsuki Kinjo<sup>1,3</sup>, Shunsaku Kitagawa<sup>1</sup>, Kenji Ishida<sup>1</sup><sup>✉</sup>, Souichiro Mizutani<sup>2</sup>, Rikako Yamamoto<sup>2</sup>, Yudai Ohmagari<sup>2</sup> & Takahiro Onimaru<sup>2</sup>

The emergence of charge-neutral fermionic excitations in magnetic systems is one of the unresolved issues in recent condensed matter physics. This type of excitations has been observed in various systems, such as low-dimensional quantum spin liquids, Kondo insulators, and antiferromagnetic insulators. Here, we report the presence of a pronounced gapless spin excitation in the low-temperature antiferromagnetic state of  $\text{YbCuS}_2$  semiconductor, where trivalent ytterbium atoms form a zigzag chain structure. We confirm the presence of this gapless excitations by a combination of experimental probes, namely  $^{63/65}\text{Cu}$ -nuclear magnetic resonance and nuclear quadrupole resonance, as well as specific heat measurements, revealing a linear low-temperature behavior of both the nuclear spin-lattice relaxation rate  $1/T_1$  and the specific heat. This system provides a platform to investigate the origin of gapless excitations in spin chains and the relationship between emergent fermionic excitations and frustration.

<sup>1</sup>Department of Physics, Kyoto University, Kyoto 606-8502, Japan. <sup>2</sup>Department of Quantum Matter, Graduate School of Advanced Science and Engineering, Hiroshima University, Higashihiroshima 739-8530, Japan. <sup>3</sup>Present address: Institute of Multidisciplinary Research for Advanced Materials, Tohoku University, Sendai, Miyagi 980-8577, Japan. ✉email: [horifumiya.36s@st.kyoto-u.ac.jp](mailto:horifumiya.36s@st.kyoto-u.ac.jp); [kishida@scphys.kyoto-u.ac.jp](mailto:kishida@scphys.kyoto-u.ac.jp)

Frustration effects in low-dimensional quantum spin systems lead to the suppression of long-range order and non-trivial ground states<sup>1</sup>. A typical example of such a frustrated quantum spin system is the  $S = 1/2$  zigzag chain with competition between the nearest-neighbor and next-nearest neighbor exchange interaction<sup>2,3</sup>. In this system, a variety of non-trivial quantum phenomena such as spin dimerization, a  $1/3$ -magnetization plateau, and vector chirality have been theoretically suggested<sup>4–6</sup> and experimentally confirmed in  $(N_2H_5)CuCl_3$ ,  $Rb_2Cu_2Mo_3O_{12}$ , and so on<sup>7–10</sup>.

Recently, there have been much attention and interest in frustrated spin systems with rare-earth elements ( $Ln$ ). The strong spin-orbit coupling (SOC) and crystalline electric field (CEF) associated with  $4f$  electrons of rare-earth ions lead to highly anisotropic exchange interactions, which gives rise to exotic states and phenomena not expected in simple  $S = 1/2$  Heisenberg theoretical models.

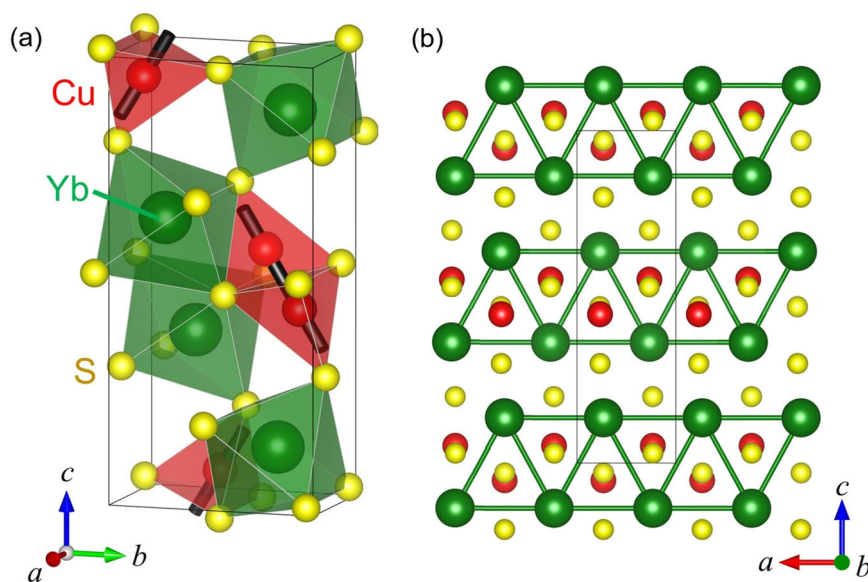
In particular, Yb-based frustrated insulators have been intensively studied<sup>11–25</sup>. Since the  $Yb^{3+}$  ion has the nearly filled  $(4f)^{13}$  configuration, the ionic states and magnetic interactions become simpler than those in a typical rare-earth ion. In addition, the CEF energy scale is relatively large, yielding an isolated CEF doublet ground state, making it suitable for exploring the physics of frustrated magnet<sup>11</sup>. For example,  $YbMgGaO_4$ <sup>12–14</sup> and  $NaYbSe_2$ <sup>15–17</sup> with a triangular structure exhibit an unusual ground state. Even though the ground state of the  $S = 1/2$  Heisenberg triangular antiferromagnets is known to be a  $120^\circ$  Neel ordered state theoretically, the spin-orbital-entangled local moments originating from  $Yb^{3+}$  ions in these compounds may host strong quantum fluctuations, stabilizing the quantum spin liquid state; a  $Z_2$  spin liquid, a Dirac-like spin liquid, or a spinon Fermi surface<sup>18–20</sup>. Moreover, Yb-based systems show often a unique ground state compared to other  $Ln$ -based systems. In fact, after the study in various  $LnCuS_2$  systems<sup>21,22</sup>, it was found that  $YbCuS_2$  has larger magnetic interactions between magnetic ions compared to other rare-earth ions. Furthermore, this compound exhibits peculiar magnetic phase diagrams such as magnetic-field-robust phase transitions and  $1/3$  plateaus, which are not seen in other rare-earth zigzag-chain materials. Quite recently, various Yb-based compounds such as  $YbCl_3$  with honeycomb lattices<sup>23</sup>,

$CdYb_2S_4$  with pyrochlore lattices<sup>24</sup>,  $SrYb_2O_4$  with zigzag chains arranged in honeycomb lattices<sup>25</sup> have also been under intense investigation.

$YbCuS_2$  is an above-mentioned Yb-based frustrated system. Figure 1a shows the crystal structure of  $YbCuS_2$ , which has an orthorhombic structure with the space group  $P2_12_12_1$  (No. 19,  $D_2^4$ ). In  $YbCuS_2$ , Yb atoms form the zigzag chains along the  $a$ -axis<sup>26</sup>. The electrical resistivity of  $YbCuS_2$  shows semiconducting behavior with an activation energy of 0.08–0.28 eV<sup>27</sup>. From the Curie-Weiss behavior of the magnetic susceptibility  $\chi(T)$ , the effective magnetic moment  $\mu_{\text{eff}}$  was estimated to be  $4.62\mu_B$ , which is close to the value of the free  $Yb^{3+}$  ion ( $4.54\mu_B$ ). In general, the CEF level is important for understanding high-temperature and high-field magnetic responses in rare-earth systems. However, the low-temperature properties are governed by only the CEF ground state which was reported to be an isolated Kramers doublet with an energy separation of about 300 K from the first excited state in  $YbCuS_2$ <sup>21,22</sup>. The negative Weiss temperature  $\theta_p = -31.6$  K considering the CEF effect indicates the antiferromagnetic (AFM) interaction between the Yb magnetic moments, which is comparable to some Yb-based systems<sup>25,28</sup>. The magnetic specific heat divided by the temperature  $C_m/T$  shows a sharp peak at  $T_O \sim 0.95$  K, suggesting a first-order (FO) phase transition. Since the transition temperature  $T_O$  is much lower than  $\theta_p$ ,  $YbCuS_2$  is expected to be a frustrated spin system. Below 20 K, the magnetic entropy decreased from  $R \ln 2$  expected for the Kramers doublet ground state. Here,  $R$  is the gas constant. The value of the magnetic entropy was only 20% of  $R \ln 2$  at  $T_O$ , suggesting that the phase transition is suppressed by the frustration effect and it causes short-range ordering above  $T_O$ .

In addition, the unusual magnetic field  $H$  dependence of  $T_O$  was reported<sup>22</sup>.  $T_O$  is independent of  $H$  up to 4 T and has a maximum at approximately 7 T. There are three anomalies in the  $H$ -swept AC susceptibility measured at low temperatures up to 18 T. These results suggest that a nontrivial ground state is realized in  $YbCuS_2$ .

To investigate the physical properties, particularly the origin of the  $T_O$  transition, from a microscopic point of view, we performed  $^{63/65}Cu$ -nuclear magnetic resonance (NMR) and nuclear quadrupole resonance (NQR) measurements on polycrystalline samples of  $YbCuS_2$ . Our NQR results indicate that the



**Fig. 1** Crystal structure. **a** Crystal structure of  $YbCuS_2$  with the space group  $P2_12_12_1$ . The black sticks represent the principal axis of the electric field gradient tensor determined by calculation using the WIEN2k package<sup>58</sup>. **b** View from the  $b$ -axis: zigzag chains along the  $a$ -axis are formed by Yb atoms. The black box represents the unit cell. The structural image was produced using the VESTA program<sup>59</sup>.

FO AFM transition occurs at  $T_O$ . Moreover, the nuclear spin-lattice relaxation rate  $1/T_1$  of  $^{63}\text{Cu}$  at zero fields abruptly decreases below  $T_O$  and exhibits  $T$ -linear behavior below 0.5 K, suggesting the presence of gapless fermionic excitations. The gapless excitations were also confirmed by the low-temperature specific-heat measurements. We discuss the possible origin of the fermionic excitation.

## Results

**$^{63/65}\text{Cu}$ -NMR/NQR spectrum.** Figure 2a shows the  $H$ -swept  $^{63/65}\text{Cu}$ -NMR spectrum measured at 4.2 K on the powdered sample. From this powder pattern of the NMR spectrum, the quadrupole parameters  $\nu_{zz}$  and  $\eta$ , which are explained subsequently, can be estimated by fitting the  $H$ -swept NMR spectrum to the calculated theoretical spectrum. In general, the total effective NMR Hamiltonian of a nucleus in  $H$  is given by

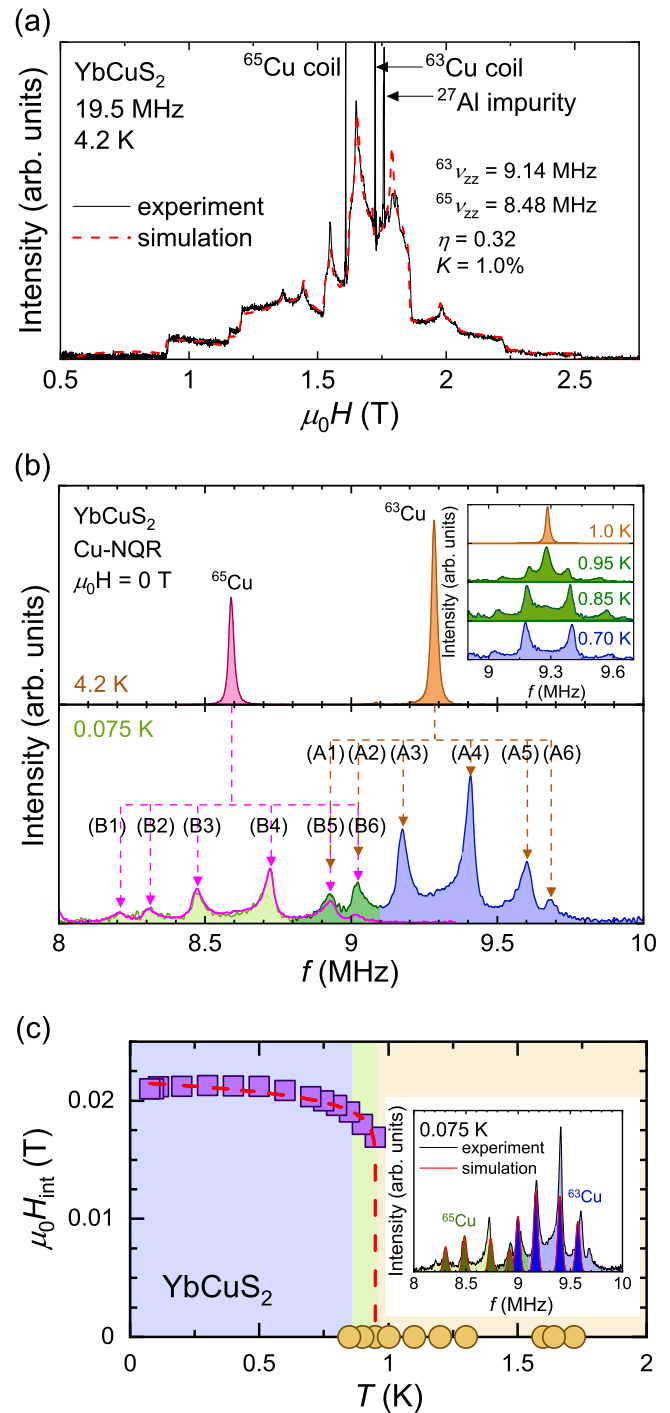
$$\mathcal{H} = \mathcal{H}_Z + \mathcal{H}_Q = -\frac{\gamma}{2\pi} h(1 + K)\mathbf{I} \cdot \mathbf{H} + \frac{h\nu_{zz}}{6} \left\{ (3I_z^2 - I^2) + \frac{1}{2}\eta(I_+^2 + I_-^2) \right\}, \quad (1)$$

where  $\gamma$  is the nuclear gyromagnetic ratio,  $K$  is the Knight shift,  $h$  is the Planck constant, and  $I_{\pm}$  are the ladder operators of the nuclear spin  $I$ , which are defined as  $I_{\pm} = I_x \pm iI_y$ .  $\nu_{zz} (\propto V_{zz})$  is the quadrupole frequency along the principal axis of the electric field gradient (EFG) and is defined as  $\nu_{zz} \equiv 3eV_{zz}Q/2I(2I - 1)$  with the electric quadrupole moment  $Q$ .  $\eta$  is an asymmetry parameter of the EFG defined as  $\eta \equiv (V_{xx} - V_{yy})/V_{zz}$ , where  $V_{ii}$  is the second derivative of the electric potential  $V$  ( $V_{ii} = \partial^2 V / \partial x_i^2$ ). Since the NMR signal of each grain depends on the angle between the principal axis of the EFG in each grain and the direction of the magnetic field, the sum of the NMR signals for all solid angles could be observed in the non-oriented powder samples. The NMR spectrum was well fitted by the simulation with  $K = 1.0\%$ ,  $^{63}\nu_{zz} = 9.14$  MHz,  $^{65}\nu_{zz} = 8.48$  MHz, and  $\eta = 0.32$ , as shown by the dashed line in Fig. 2a.

We observed sharp  $^{63/65}\text{Cu}$ -NQR signals at  $^{63}\nu_Q = 9.28$  MHz and  $^{65}\nu_Q = 8.59$  MHz, as shown in the upper panel of Fig. 2b. The spectra were obtained by the frequency-swept method at 4.2 K without an external field. The obtained  $^{63/65}\text{Cu}$ -NQR frequencies  $\nu_Q$  at 4.2 K were consistently reproduced by  $\nu_Q = \nu_{zz} \sqrt{1 + \eta^2/3}$  with the quadrupole parameters obtained above.

The occurrence of the AFM transition at  $T_O$  was concluded from the following NQR results. The lower panel of Fig. 2b shows the frequency-swept  $^{63/65}\text{Cu}$ -NQR spectra measured at 0.075 K. Each paramagnetic (PM) peak splits into six peaks [(A1)–(A6) for  $^{63}\text{Cu}$  and (B1)–(B6) for  $^{65}\text{Cu}$ ]. The  $^{63}\text{Cu}$  signals for (A1) and (A2) overlap with the  $^{65}\text{Cu}$  signals for (B5) and (B6), respectively. As shown in Fig. 2b, the observed  $^{65}\text{Cu}$  peaks almost coincide with the  $^{63}\text{Cu}$  signals scaled by the isotope ratio of the nuclear gyromagnetic ratio  $^{65}\gamma/^{63}\gamma = 1.07$ , not by that of the quadrupole moment  $^{65}Q/^{63}Q = 0.93$ . In addition, since the  $^{63}\nu_Q$  does not change across  $T_O$ , the EFG parameters seem to be unchanged below  $T_O$  (see Supplementary Note 1). Therefore, the NQR signals are split due to the appearance of internal magnetic fields at the Cu site rather than to the change of electric factors such as charge density wave, charge-ordered, or structural transitions.

We performed spectrum simulations to estimate the magnitude of the internal magnetic fields and their orientation with respect to the principal axis of the EFG at 0.075 K. As shown in the inset of Fig. 2c, the eight clearly visible peaks (A2)–(A5) and (B2)–(B5) can be fitted by the simulation with  $\mu_0 H_{\text{int}} = 0.021$  T,  $\theta = 77^\circ$ , and  $\phi = 0^\circ$ , where  $\mu_0 H_{\text{int}}$  is the absolute value of the internal fields,  $\theta$  is



**Fig. 2**  $^{63/65}\text{Cu}$ -NMR/NQR spectrum. **a** NMR spectrum at a fixed frequency of 19.5 MHz and 4.2 K: the black solid and red dashed curves are the experimental result and the simulation of the NMR spectrum, respectively. The three narrow lines in the NMR spectrum are signals from the Cu coil used for the NMR measurements and Al as an impurity arising from the NMR probe. **b**  $^{63/65}\text{Cu}$ -NQR spectra at 4.2 and 0.075 K: the pink curve represents the  $^{63}\text{Cu}$  signals scaled by  $^{65}\gamma/^{63}\gamma$  and shifted to the observed  $^{65}\text{Cu}$  signals. The inset shows the temperature variations of the  $^{63}\text{Cu}$ -NQR spectrum for  $0.7 \leq T \leq 1.0$  K. **c** Temperature dependence of the internal fields  $H_{\text{int}}$  estimated by simulation of the NQR spectra: the red dashed curve represents the relation  $H_{\text{int}}(T) = H_{\text{int}}(0)[(T_O - T)/T_O]^\beta$  with  $\beta = 0.05$ . The inset shows the  $^{63/65}\text{Cu}$ -NQR spectrum at 0.075 K, and the red solid curve is the simulation of the NQR spectrum.

the polar angle, and  $\phi$  is the azimuthal angle of the internal fields from the principal axis of the EFG. The small internal field at the Cu site suggests the tiny Yb-ordered moment (see Supplementary Note 2). However, the peaks (A1), (A6), (B1), and (B6) cannot be fitted by the above parameters: these peaks can be reproduced by assuming a slightly larger internal field. Moreover, the presence of non-zero intensity between the peaks indicates the distribution of the internal fields (see Supplementary Note 2). The wide distribution of the internal fields suggests that the ground state is incommensurate spiral or spin-density wave (SDW)-type magnetic order. Thus, to determine the realized magnetic structure, elastic neutron scattering measurements are necessary.

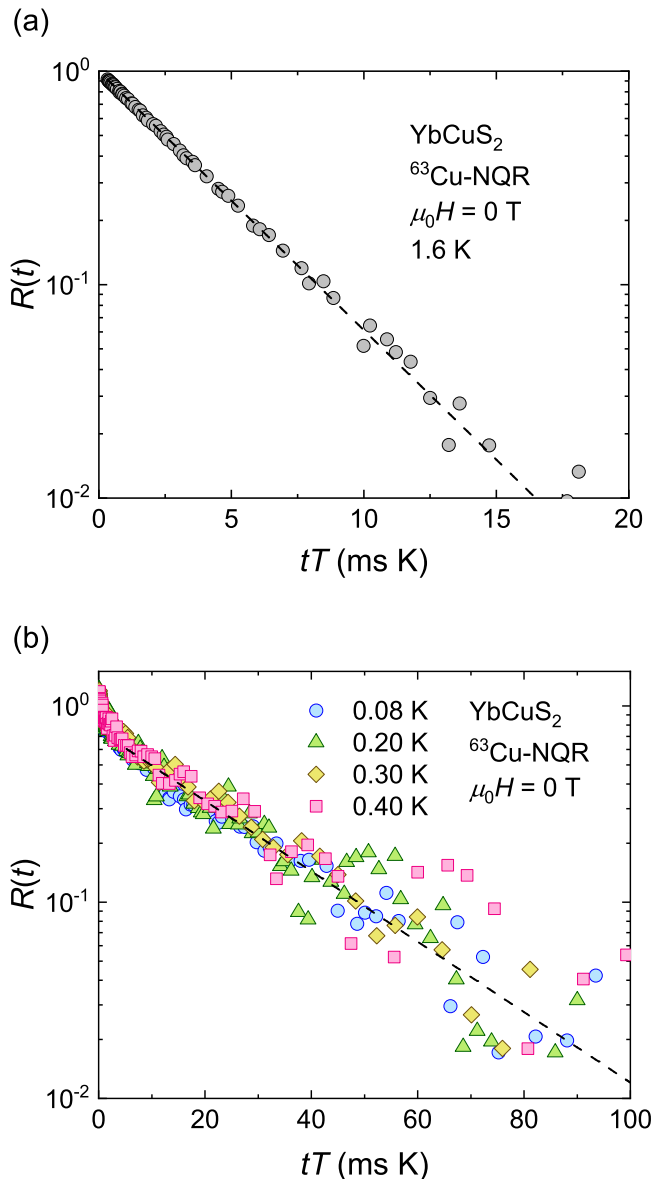
The inset of Fig. 2b shows the temperature variations in the  $^{63}\text{Cu}$ -NQR spectra below 1.0 K. Multi-peaks appear below  $T_O \sim 0.95$  K and coexist with the PM peak of  $\nu_Q = 9.28$  MHz. The PM peak is not visible below 0.85 K. As shown in the main figure of Fig. 2c, the internal field evaluated with the above simulation of the NQR spectra increases discontinuously below  $T_O$ , and the critical exponent  $\beta$  derived by fitting the relation  $H_{\text{int}}(T) = H_{\text{int}}(0)[(T_O - T)/T_O]^\beta$  is 0.05, which is substantially smaller than the conventional mean-field value (0.5). These results indicate that the AFM transition is an FO phase transition, which is consistent with the sharp peak at  $T_O$  in the specific heat<sup>22</sup>. The FO AFM transition is unusual and has been observed when the AFM transition and structural transition occur simultaneously<sup>29,30</sup>. In  $\text{YbCuS}_2$ , since the NQR parameters are unchanged below  $T_O$ , a structural transition is unlikely. Therefore, the FO AFM transition is likely to be related to magnetic frustration. In fact, fluctuation-induced FO AFM transitions have been proposed from theoretical studies<sup>31,32</sup> and several frustrated magnets such as  $\text{EuPtSi}$  show an FO AFM transition without a structural phase transition<sup>33,34</sup>. The magnetic properties of  $\text{YbCuS}_2$  deserve further investigation with various measurements.

**Nuclear spin-lattice relaxation rate  $1/T_1$ .** The nuclear spin-lattice relaxation rate  $1/T_1$  of  $^{63/65}\text{Cu}$ -NQR was measured in order to investigate the magnetic fluctuations at low temperatures. Figure 3 shows the typical relaxation curves  $R(t) \equiv 1 - M(t)/M_0$  of the nuclear magnetization  $M(t)$  at (a)  $T = 1.6$  K ( $>T_O$ ) and (b)  $T \leq 0.4$  K ( $<T_O$ ), and the fitting for  $T_1$  determination. As shown in Fig. 3a, the single exponential function of

$$R(t) = \exp\left(-\frac{3t}{T_1}\right) \quad (2)$$

was used as the fitting function above  $T_O$ .  $R(t)$  has not only a major slow component but also a minor fast component below  $T_O$  as shown in Fig. 3b. The two components seem to originate from the distribution of the relaxation in the magnetically ordered state. The slow and fast components were determined by fitting two decay regions of  $R(t)$  with the single exponential function (the fast component was determined with the decay from  $R(0)$  to  $0.7R(0)$  as shown in Supplementary Note 3). As the fraction of the slowest component become dominant below  $T_O$ , we picked up the slow component fitted by the single exponential function below  $0.7R(0)$ , and we plotted the  $1/T_1$  data.

Figure 4 shows the temperature dependence of the nuclear spin-lattice relaxation rate  $1/T_1$  measured at the  $^{63}\text{Cu}$  signal of  $\text{YbCuS}_2$ . Below  $T_O$ ,  $1/T_1$  was measured at the two peaks shown in the inset. To investigate contributions other than the  $4f$  electrons, we also measured  $1/T_1$  of a nonmagnetic reference compound  $\text{LuCuS}_2$  and plot the results. For  $\text{LuCuS}_2$ , the isotopic ratio of  $1/T_1$  [ $^{65}(1/T_1)/^{63}(1/T_1)$ ] is 0.88, which is close to the square of the quadrupole-moment ratio ( $^{65}Q/^{63}Q$ )<sup>2</sup>  $\sim 0.86$ . This indicates that in  $\text{LuCuS}_2$ ,  $1/T_1$  is



**Fig. 3  $^{63}\text{Cu}$  relaxation curve.**  $^{63}\text{Cu}$  relaxation curve  $R(t)$  at **a**  $T = 1.6$  K ( $>T_O$ ) and **b**  $T \leq 0.4$  K ( $<T_O$ ). The dashed line represents the fitting of the slow component.

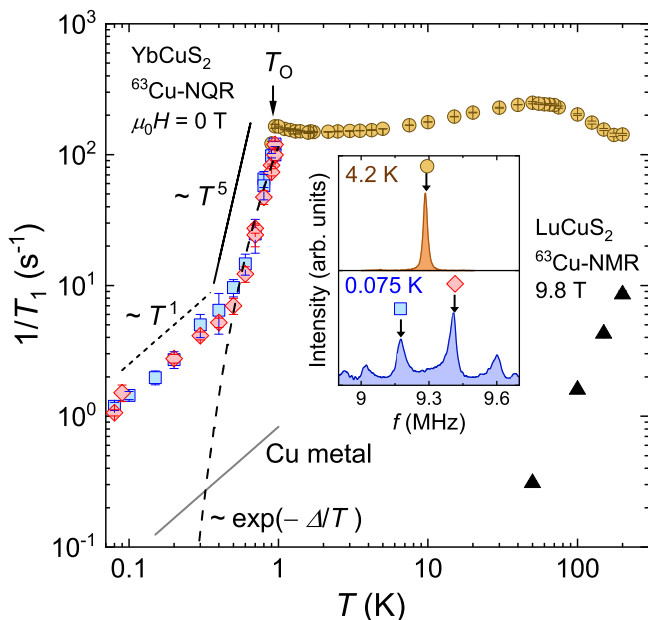
determined by the electric quadrupole relaxation originating from the phonon dynamics. The low-temperature  $1/T_1$  of  $\text{LuCuS}_2$  is quite small. In contrast, for  $\text{YbCuS}_2$ , the isotopic ratio of  $1/T_1 \sim 1.14$  coincides with the square of the gyromagnetic ratios ( $^{65}\gamma/^{63}\gamma$ )<sup>2</sup>  $\sim 1.15$ , indicating that  $1/T_1$  is determined by the magnetic relaxation from the  $\text{Yb}^{3+}$  moments.  $1/T_1$  exhibits a broad maximum at  $\sim 50$  K, where the magnetic entropy reaches  $R \ln 2$ , as expected for the Kramers doublet ground state in specific-heat measurements. Note that  $1/T_1$  gradually decreases below 50 K. This may be related to the entropy release observed in the specific-heat measurements, which is described later. Below 5 K,  $1/T_1$  becomes constant, suggesting that the local moments fluctuate with a short-range correlation. This behavior agrees with the theoretical prediction for the one-dimensional (1-D) spin chain<sup>35</sup>, and it was observed in the  $S = 1/2$  1-D cuprate antiferromagnet<sup>36,37</sup>. On the other hand, the absence of the critical slowing down behavior around  $T_O$  is in sharp contrast to the divergence behavior of  $1/T_1$  observed in the zigzag chain compound  $\text{CaV}_2\text{O}_4$ <sup>38</sup> and the above 1-D



cuprate antiferromagnets near  $T_N$ <sup>36,37</sup>, where the magnetic order occurs due to interchain coupling. The absence of the slowing down behavior is likely to be related to the character of the FO phase transition<sup>30</sup>.

Below  $T_O$ ,  $1/T_1$  decreases rapidly; it is roughly proportional to  $T^5$  down to 0.5 K. In general,  $1/T_1$  of local-moment frustrated systems, such as the triangular Heisenberg antiferromagnet, is determined by the two-magnon process. It can be expressed as  $1/T_1 \propto T^{2D-1}$  for  $T \gg \Delta$ , where  $\Delta$  is the spin gap, and  $D$  ( $=3$  or  $2$ ) is the dimensionality of the spin-wave dispersion<sup>39–42</sup>. In  $\text{YbCuS}_2$ ,  $D = 3$  is likely. Conversely, peculiar  $T$ -linear behavior was observed below 0.5 K. Theoretically,  $1/T_1$  decreases exponentially [ $1/T_1 \sim \exp(-\Delta/T)$ ] for  $T \ll \Delta$  at low temperatures in conventional semiconducting antiferromagnets with a spin gap<sup>39,40</sup>. Thus, the  $T$ -linear behavior suggests the presence of gapless excitation, which makes  $\text{YbCuS}_2$  quite different from conventional antiferromagnets.

**Specific heat.** In addition to the previous study of the magnetic susceptibility<sup>22</sup>, we further studied the CEF levels and magnetic interaction from the magnetic specific heat  $C_m$  and the magnetic entropy  $S_m$  by using the specific heat of  $\text{LuCuS}_2$ . The specific heat of  $\text{LuCuS}_2$  would be more reliable and accurate for the lattice contribution than that of  $\text{YCuS}_2$  in the previous study<sup>22</sup>, because the ionic radius of Lu is closer to that of Y than that of Y. As shown in the inset of Fig. 5, a broad maximum of  $C_m/T$  was also observed near 100 K, which is reproduced by a two-level model with the energy separations of 300 K from the doublet ground state to the first excited quartet. Moreover, the magnetic entropy  $S_m$  reaches  $R \ln 2$  at higher temperatures near 50 K, which is likely related to a broad maximum near 50 K of  $1/T_1$  in the

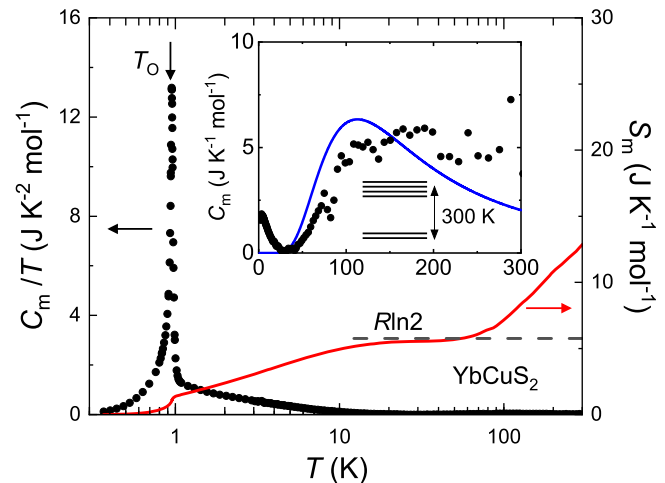


**Fig. 4 Nuclear spin-lattice relaxation rate  $1/T_1$ .** Temperature dependence of the nuclear spin-lattice relaxation rates  $1/T_1$  of  $\text{YbCuS}_2$  and a nonmagnetic reference compound  $\text{LuCuS}_2$ : the circles denote the  $^{63}\text{Cu}$ -NQR  $1/T_1$  in the PM state of  $\text{YbCuS}_2$ . The diamonds and squares represent  $1/T_1$  in the AFM state of  $\text{YbCuS}_2$ . The black triangles indicate  $^{63}\text{Cu}$ -NMR  $1/T_1$  in  $\text{LuCuS}_2$  for  $\mu_0 H = 9.8$  T. The gray solid line denotes  $1/T_1$  in a Cu-metal<sup>47</sup>. The dashed curve represents  $1/T_1 \sim \exp(-\Delta/T)$  in conventional semiconducting antiferromagnets with a spin gap. The inset shows the  $^{63}\text{Cu}$ -NQR spectra measured at 4.2 and 0.075 K. The spectrum peaks at which  $1/T_1$  was measured are denoted by the symbols. Error bars are standard deviations.

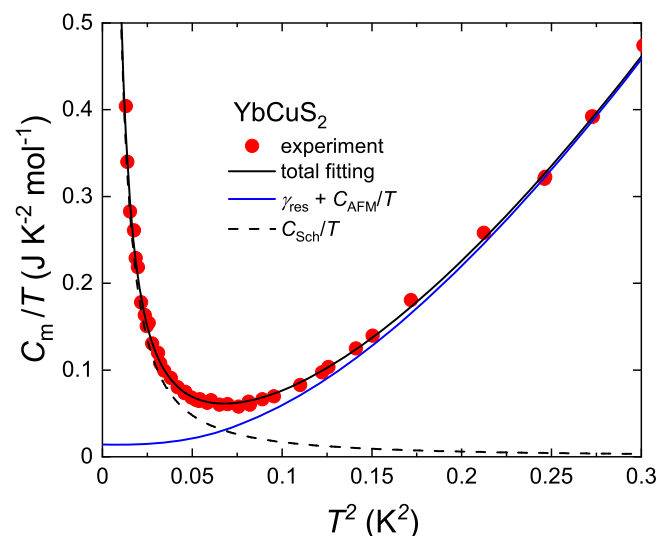
NQR measurement. Theoretically,  $1/T_1$  increases towards the temperature corresponding to the energy scale of the interaction<sup>43</sup>. Hence, the isolated CEF doublet ground state and the strong interactions between Yb moments are convincing in  $\text{YbCuS}_2$ .

The presence of the gapless excitation was also confirmed from the low- $T$  specific-heat measurements. The specific heat measurements and the analysis of the residual  $T$ -linear term  $\gamma_{\text{el}}$  of specific heat were performed down to 0.08 K as shown in Fig. 6.  $C_m$  can be fitted by

$$\frac{C_m}{T} = \gamma_{\text{res}} + \frac{C_{\text{AFM}}}{T} + \frac{C_{\text{Sch}}}{T}. \quad (3)$$



**Fig. 5 Specific heat and entropy.** Temperature dependence of magnetic specific heat  $C_m$  divided by the temperature (left-hand scale) and magnetic entropy  $S_m$  (right-hand scale) for  $\text{YbCuS}_2$ .  $C_m$  was estimated by the subtraction of the lattice contribution measured in  $\text{LuCuS}_2$ . The inset shows the temperature dependence of magnetic specific heat  $C_m$ . The blue solid line is a fit with a two-level model with the energy separations of 300 K from the doublet ground state to the first excited quartet.



**Fig. 6 Low-temperature specific heat.** Temperature dependence of magnetic specific heat  $C_m$  divided by temperature. The black solid, blue solid, and black dashed curves represent the total fitting, the residual term  $\gamma_{\text{res}} + \text{AFM}$  magnon contribution, and the Schottky contribution, respectively.

**Table 1 Parameters obtained from the specific heat analysis at low temperatures.**

$\gamma_{\text{res}}$ (mJ K <sup>-2</sup> mol <sup>-1</sup> )	$\beta$ (mJ K <sup>-4</sup> mol <sup>-1</sup> )	$\Delta_{\text{m}}$ (K)	$\Delta_{\text{nuc}}$ (K)
14(2)	7.4(6)	0.89(4)	0.0160(1)

Here, the second term represents AFM magnon excitations with an energy gap  $\Delta_{\text{m}}$ <sup>44</sup>

$$\frac{C_{\text{AFM}}}{T} = \beta T^2 \exp\left(-\frac{\Delta_{\text{m}}}{T}\right). \quad (4)$$

The third term is the two-level nuclear Schottky term

$$\begin{aligned} \frac{C_{\text{Sch}}}{T} = & \frac{R\Delta_{\text{Cu}}^2}{T^3} \frac{e^{-\Delta_{\text{Cu}}/T}}{(1 + e^{-\Delta_{\text{Cu}}/T})^2} \\ & + \frac{R\Delta_{\text{nuc}}^2}{T^3} \frac{e^{-\Delta_{\text{nuc}}/T}}{(1 + e^{-\Delta_{\text{nuc}}/T})^2}, \end{aligned} \quad (5)$$

where  $\Delta_{\text{Cu}}$  and  $\Delta_{\text{nuc}}$  are the corresponding energy splitting of Cu nucleus and other nucleus (Yb and S), respectively. Using the energy splitting of Cu nucleus  $\Delta_{\text{Cu}} = 4.37$  mK estimated from NQR measurements, this analysis yields the parameters as listed in Table 1. This analysis shows the residual term  $\gamma_{\text{res}} = 14$  mJ K<sup>-2</sup> mol<sup>-1</sup>. While  $\gamma_{\text{res}}$  term is usually defined as an electronic specific-heat term in metallic compounds, it may be attributed to gapless excitation with a pseudo-Fermi surface.

## Discussion

The presence of gapless quasiparticle excitation on an incommensurate antiferromagnetic ordered state with a tiny ordered moment in YbCuS<sub>2</sub> is not consistent with the simple  $S = 1/2$  Heisenberg zigzag-chain antiferromagnet model, in which a Tomonaga–Luttinger liquid or a gapped dimer phase were expected at zero magnetic field<sup>4–6</sup>. There is a possibility that exotic ground state and quasiparticle excitation in YbCuS<sub>2</sub> originate from the anisotropic interactions unique to the effect of SOC and CEF of  $4f$  electrons. The specific heat and  $1/T_1$  measurements under magnetic fields to investigate the low- $T$  properties are interesting since the peculiar magnetic field-temperature phase diagram was reported.

Here, we discuss the origin of the gapless excitation. The similar  $T$ -linear behavior of  $1/T_1$  was reported in kagomé systems, Zn-brochantite ZnCu<sub>3</sub>(OH)<sub>6</sub>SO<sub>4</sub> below the nonmagnetic phase transition<sup>45</sup> and volborthite Cu<sub>3</sub>V<sub>2</sub>O<sub>7</sub>(OH)<sub>2</sub>·2H<sub>2</sub>O below the magnetic phase transition<sup>46</sup>. To explain these behaviors, particle-hole excitations by spinons (fermionic elementary excitations), which are analogous to metallic excitations, were proposed<sup>45,46</sup>. In fact, we point out that the experimental value of  $1/T_1 T$  in YbCuS<sub>2</sub> at 0.1 K ( $\sim 14$  s<sup>-1</sup> K<sup>-1</sup>) is larger than that in a Cu-metal ( $\sim 0.83$  s<sup>-1</sup> K<sup>-1</sup>)<sup>47</sup> by more than one order of magnitude.

Another possibility is *phason* excitation<sup>48–51</sup>.  $T$ -linear  $1/T_1$  was observed in the temperature region just below  $T_{\text{SDW}}$  in organic quasi 1-D metallic (TMTSF)<sub>2</sub>PF<sub>6</sub>, and this  $1/T_1$  behavior was interpreted with the gapless phason contribution in the incommensurate SDW state<sup>48–50</sup>. Here, the phason is elementary excitation corresponding to phase mode<sup>51</sup>. There is a possibility that the gapless excitation in YbCuS<sub>2</sub> originates from such an unusual excitation, but it is surprising that such behavior was observed in semiconducting YbCuS<sub>2</sub>.

Quite recently, gapless excitation has been observed in Yb-based semiconducting Kondo-lattice materials such as YbB<sub>12</sub><sup>52–54</sup> and YbIr<sub>3</sub>Si<sub>7</sub><sup>55</sup>. In these compounds, although the band gap opens at low temperatures due to the hybridization between the localized  $f$  and the conduction electrons, quantum oscillation at high

fields and the finite residual term in the specific heat and thermal conductivity experiments were observed<sup>53,55</sup>. These results suggest the presence of gapless and charge-neutral excitations in the bulk properties, which are proposed to result in a quantum spin liquid with a spinon Fermi surface and the Majorana Fermi liquid<sup>56,57</sup>. We note the possibility that the large gapless excitation observed at low temperatures in YbCuS<sub>2</sub> might arise from such exotic Fermi liquid states, although YbCuS<sub>2</sub> is a conventional semiconductor. To confirm this possibility, it is crucially important to prepare high-quality single crystals for the measurements of thermal conductivity and quantum oscillation.

## Conclusion

In conclusion, we performed <sup>63/65</sup>Cu-NMR/NQR and specific-heat measurements on polycrystalline samples of YbCuS<sub>2</sub> in which the Yb ions form a zigzag chain along the orthorhombic  $a$ -axis. Below  $T_{\text{O}} \sim 0.95$  K, multi-peaks affected by the internal magnetic fields appear; they coexist with the PM signal down to 0.85 K, indicating that the FO AFM phase transition occurs at  $T_{\text{O}}$ . In addition,  $1/T_1$  decreases abruptly below  $T_{\text{O}}$  and exhibits  $T$ -linear behavior below 0.5 K. The significantly large  $1/T_1 T$  value—more than one order of magnitude larger than that for metallic Cu suggests the presence of gapless spin excitation originating from exotic fermions, which was also confirmed by the low- $T$  specific heat measurements. Our finding of the large gapless excitation unveils the presence of unknown fermionic quasiparticles in frustrated magnets.

## Methods

**<sup>63/65</sup>Cu-NMR/NQR measurements.** Polycrystalline samples of YbCuS<sub>2</sub> were synthesized by the melt-growth method<sup>21,22</sup>. The polycrystalline samples were coarsely powdered to increase the surface area for better thermal contact. The powdered sample was mixed with GE 7031 varnish and solidified at zero magnetic fields to avoid the preferential orientation of crystals for the NMR measurements and contact between crystals for the NQR measurements. A conventional spin-echo technique was used for the NMR and NQR measurements. A <sup>3</sup>He–<sup>4</sup>He dilution refrigerator was used for the NQR measurements down to 0.075 K. The stability of the temperature is about  $\pm 5$  mK, and the typical measurement time for one spectrum is about 2–3 h. The NQR measurement was performed in the cooling process. <sup>63/65</sup>Cu-NMR spectra (with nuclear gyromagnetic ratios of <sup>63</sup>γ/ $2\pi = 11.289$  and <sup>65</sup>γ/ $2\pi = 12.093$  MHz T<sup>-1</sup>, respectively, and both with the nuclear spin  $I = 3/2$ ) were obtained as a function of  $H$  at the frequency  $f = 19.5$  MHz. The principal axis of the EFG at the Cu site was determined by WIEN2k calculation using the density functional theory<sup>58</sup> since the principal axis was not determined experimentally due to a lack of a single crystal sample. The principal axis is represented by the black sticks in Fig. 1a. <sup>63/65</sup>Cu- $1/T_1$  was measured in YbCuS<sub>2</sub> and a reference compound LuCuS<sub>2</sub> to estimate the lattice contribution.  $1/T_1$  was evaluated by fitting the relaxation curve of the nuclear magnetization after the saturation to a theoretical function for the nuclear spin  $I = 3/2$ .  $1/T_1$  can be determined by a single relaxation component down to  $T_{\text{O}}$ . However, a short component appears in the relaxation curve below  $T_{\text{O}}$ , thus, we picked up the slowest components.

**Specific-heat measurements.** Specific-heat measurements were performed on a polycrystalline sample of 4.74 mg down to 0.08 K by the thermal relaxation method with a Quantum Design PPMS and mF-ADR-100s.

## Data availability

The data that support the findings of this study are available from the corresponding author upon reasonable request.

## Code availability

The analysis code for this study is available from the corresponding authors upon reasonable request.

Received: 21 December 2022; Accepted: 27 June 2023;

Published online: 21 July 2023

## References

- Balents, L. Spin liquids in frustrated magnets. *Nature* **464**, 199 (2010).
- Majumdar, C. K. & Ghosh, D. K. On next-nearest-neighbor interaction in linear chain. II. *J. Math. Phys.* **10**, 1399 (1969).
- Haldane, F. D. M. Spontaneous dimerization in the  $S = 1/2$  Heisenberg antiferromagnetic chain with competing interactions. *Phys. Rev. B* **25**, 4925 (1982).
- Okunishi, K. & Tonegawa, T. Magnetic phase diagram of the  $S = 1/2$  antiferromagnetic zigzag spin chain in the strongly frustrated region: cusp and plateau. *J. Phys. Soc. Jpn.* **72**, 479 (2003).
- Hikihara, T., Kecke, L., Momoi, T. & Furusaki, A. Vector chiral and multipolar orders in the spin- $\frac{1}{2}$  frustrated ferromagnetic chain in magnetic field. *Phys. Rev. B* **78**, 144404 (2008).
- Hikihara, T., Momoi, T., Furusaki, A. & Kawamura, H. Magnetic phase diagram of the spin- $\frac{1}{2}$  antiferromagnetic zigzag ladder. *Phys. Rev. B* **81**, 224433 (2010).
- Maeshima, N. et al. Magnetic properties of a  $S = 1/2$  zigzag spin chain compound  $(\text{N}_2\text{H}_5)_2\text{CuCl}_2$ . *J. Phys. Condens. Matter* **15**, 3607 (2003).
- Hase, M. et al. Magnetic properties of  $\text{Rb}_2\text{Cu}_2\text{Mo}_3\text{O}_{12}$  including a one-dimensional spin-12 Heisenberg system with ferromagnetic first-nearest-neighbor and antiferromagnetic second-nearest-neighbor exchange interactions. *Phys. Rev. B* **70**, 104426 (2004).
- Furukawa, S., Sato, M. & Onoda, S. Chiral order and electromagnetic dynamics in one-dimensional multiferroic cuprates. *Phys. Rev. Lett.* **105**, 257205 (2010).
- Pregelj, M. et al. Spin-stripe phase in a frustrated zigzag spin-1/2 chain. *Nat. Commun.* **6**, 7255 (2015).
- Rau, J. G. & Gingras, M. J. P. Frustration and anisotropic exchange in ytterbium magnets with edge-shared octahedra. *Phys. Rev. B* **98**, 054408 (2018).
- Li, Y. et al. Gapless quantum spin liquid ground state in the two-dimensional spin-1/2 triangular antiferromagnet  $\text{YbMgGaO}_4$ . *Sci. Rep.* **5**, 16419 (2015).
- Li, Y. et al. Rare-earth triangular lattice spin liquid: a single-crystal study of  $\text{YbMgGaO}_4$ . *Phys. Rev. Lett.* **115**, 167203 (2015).
- Li, Y. et al. Muon spin relaxation evidence for the  $U(1)$  quantum spin-liquid ground state in the triangular antiferromagnet  $\text{YbMgGaO}_4$ . *Phys. Rev. Lett.* **117**, 097201 (2016).
- Liu, W. et al. Rare-earth chalcogenides: a large family of triangular lattice spin liquid candidates. *Chin. Phys. Lett.* **35**, 117501 (2018).
- Ranjith, K. M. et al. Anisotropic field-induced ordering in the triangular-lattice quantum spin liquid  $\text{NaYbSe}_2$ . *Phys. Rev. B* **100**, 224417 (2019).
- Dai, P.-L. et al. Spinon fermi surface spin liquid in a triangular lattice antiferromagnet  $\text{NaYbSe}_2$ . *Phys. Rev. X* **11**, 021044 (2021).
- Li, Y.-D., Wang, X. & Chen, G. Anisotropic spin model of strong spin-orbit-coupled triangular antiferromagnets. *Phys. Rev. B* **94**, 035107 (2016).
- Li, Y.-D., Lu, Y.-M. & Chen, G. Spinon fermi surface  $U(1)$  spin liquid in the spin-orbit-coupled triangular-lattice mott insulator  $\text{YbMgGaO}_4$ . *Phys. Rev. B* **96**, 054445 (2017).
- Zhu, Z., Maksimov, P. A., White, S. R. & Chernyshev, A. L. Topography of spin liquids on a triangular lattice. *Phys. Rev. Lett.* **120**, 207203 (2018).
- Ohmagari, Y. et al. Magnetic properties of rare-earth sulfides  $\text{RCuS}_2$  ( $R = \text{Dy}, \text{Ho}, \text{Er}, \text{Tm}, \text{and Yb}$ ). *JPS Conf. Proc.* **30**, 011167 (2020).
- Ohmagari, Y. et al. Quantum phase transitions in an Yb-based semiconductor  $\text{YbCuS}_2$  with an effective spin-1/2 zigzag chain. *J. Phys. Soc. Jpn.* **89**, 093701 (2020).
- Xing, J. et al. Néel-type antiferromagnetic order and magnetic field-temperature phase diagram in the spin- $\frac{1}{2}$  rare-earth honeycomb compound  $\text{YbCl}_3$ . *Phys. Rev. B* **102**, 014427 (2020).
- Higo, T. et al. Frustrated magnetism in the Heisenberg pyrochlore antiferromagnets  $\text{AYb}_2\text{X}_4$  ( $A = \text{Cd}, \text{Mg}; X = \text{S}, \text{Se}$ ). *Phys. Rev. B* **95**, 174443 (2017).
- Quintero-Castro, D. L. et al. Coexistence of long- and short-range magnetic order in the frustrated magnet  $\text{SrYb}_2\text{O}_4$ . *Phys. Rev. B* **86**, 064203 (2012).
- Gulay, L. D. & Olekseyuk, I. D. Crystal structures of the compounds  $\text{RCuS}_2$  ( $R = \text{Dy}, \text{Ho}, \text{Yb}, \text{Lu}$ ) and  $\text{Tm}_{0.97}\text{Cu}_{1.10}\text{S}_2$ . *J. Alloys Compd.* **402**, 89 (2005).
- Murugesan, T. & Gopalakrishnan, J. Rare earth copper sulphides ( $\text{LnCuS}_2$ ). *Indian J. Chem.* **22A**, 469 (1983).
- Iizuka, R., Numakura, R., Michimura, S., Katano, S. & Kosaka, M. Magnetic properties of rare-earth sulfide  $\text{YbAgS}_2$ . *Physica B: Condens. Matter* **536**, 314–316 (2018).
- Rotter, M. et al. Spin-density-wave anomaly at 140 K in the ternary iron arsenide  $\text{BaFe}_2\text{As}_2$ . *Phys. Rev. B* **78**, 020503 (2008).
- Baek, S.-H. et al. First-order magnetic transition in single-crystalline  $\text{CaFe}_2\text{As}_2$  detected by  $^{75}\text{As}$  nuclear magnetic resonance. *Phys. Rev. B* **79**, 052504 (2009).
- Bak, P., Krinsky, S. & Mukamel, D. First-order transitions, symmetry, and the  $\epsilon$  expansion. *Phys. Rev. Lett.* **36**, 52 (1976).
- Vojta, M. Frustration and quantum criticality. *Rep. Prog. Phys.* **81**, 064501 (2018).
- Franco, D. G., Prots, Y., Geibel, C. & Seiro, S. Fluctuation-induced first-order transition in Eu-based trillium lattices. *Phys. Rev. B* **96**, 014401 (2017).
- Sakakibara, T. et al. Fluctuation-induced first-order transition and tricritical point in  $\text{EuPtSi}$ . *J. Phys. Soc. Jpn.* **88**, 093701 (2019).
- Sachdev, S. NMR relaxation in half-integer antiferromagnetic spin chains. *Phys. Rev. B* **50**, 13006 (1994).
- Ishida, K. et al. Spin correlation and spin gap in quasi-one-dimensional spin-1/2 cuprate oxides: a  $^{63}\text{Cu}$  NMR study. *Phys. Rev. B* **53**, 2827 (1996).
- Takigawa, M., Motoyama, N., Eisaki, H. & Uchida, S. Dynamics in the  $S = 1/2$  one-dimensional antiferromagnet  $\text{Sr}_2\text{CuO}_3$  via  $^{63}\text{Cu}$  NMR. *Phys. Rev. Lett.* **76**, 4612 (1996).
- Zong, X. et al.  $^{17}\text{O}$  and  $^{51}\text{V}$  NMR for the zigzag spin-1 chain compound  $\text{CaV}_2\text{O}_4$ . *Phys. Rev. B* **77**, 014412 (2008).
- Moriya, T. Nuclear magnetic relaxation in antiferromagnetics. *Prog. Theor. Phys.* **16**, 23 (1956).
- Moriya, T. Nuclear magnetic relaxation in antiferromagnetics, II. *Prog. Theor. Phys.* **16**, 641 (1956).
- Maegawa, S. Nuclear magnetic relaxation and electron-spin fluctuation in a triangular-lattice Heisenberg antiferromagnet  $\text{CsNiBr}_3$ . *Phys. Rev. B* **51**, 15979 (1995).
- Takeya, H. et al. Spin dynamics and spin freezing behavior in the two-dimensional antiferromagnet  $\text{NiGa}_2\text{S}_4$  revealed by Ga-NMR, NQR and  $\mu\text{SR}$  measurements. *Phys. Rev. B* **77**, 054429 (2008).
- Sandvik, A. W. NMR relaxation rates for the spin-1/2 Heisenberg chain. *Phys. Rev. B* **52**, R9831 (1995).
- Bredl, C. D. Specific heat of heavy fermions in Ce-based Kondo-lattices at very low temperatures. *J. Magn. Magn. Mater.* **63–64**, 355–357 (1987).
- Gomilšek, M. et al. Field-induced instability of a gapless spin liquid with a spinon Fermi surface. *Phys. Rev. Lett.* **119**, 137205 (2017).
- Yoshida, M., Takigawa, M., Yoshida, H., Okamoto, Y. & Hiroi, Z. Phase diagram and spin dynamics in volborthite with a distorted kagome lattice. *Phys. Rev. Lett.* **103**, 077207 (2009).
- Carter, G. C., Bennett, L. H. & Kahan, D. J. *Metallic Shifts in NMR*. Part I (Pergamon, London, 1977).
- Valfells, S. et al. Spin-density-wave state in  $(\text{TMTSF})_2\text{PF}_6$ : a  $^{77}\text{Se}$  NMR study at high magnetic fields. *Phys. Rev. B* **56**, 2585–2593 (1997).
- Clark, W. et al. NMR as a probe of incommensurate spin density waves in organic metals. *Synth. Met.* **86**, 1941–1947 (1997).
- Brown, S. E., Clark, W. G. & Kriza, G. Relation between the dielectric function and nuclear spin-lattice relaxation by thermal phase fluctuations of a pinned spin-density wave. *Phys. Rev. B* **56**, 5080–5083 (1997).
- Starykh, O. A. & Balents, L. Excitations and quasi-one-dimensionality in field-induced nematic and spin density wave states. *Phys. Rev. B* **89**, 104407 (2014).
- Xiang, Z. et al. Quantum oscillations of electrical resistivity in an insulator. *Science* **362**, 65–69 (2018).
- Sato, Y. et al. Unconventional thermal metallic state of charge-neutral fermions in an insulator. *Nat. Phys.* **15**, 954 (2019).
- Xiang, Z. et al. Unusual high-field metal in a Kondo insulator. *Nat. Phys.* **17**, 788–793 (2021).
- Sato, Y. et al. Charge neutral fermions and magnetic field driven instability in insulating  $\text{YbIr}_3\text{Si}_7$ . *Nat. Commun.* **13**, 394 (2022).
- Chowdhury, D., Sodemann, I. & Senthil, T. Mixed-valence insulators with neutral Fermi surfaces. *Nat. Commun.* **9**, 1766 (2018).
- Varma, C. M. Majoranas in mixed-valence insulators. *Phys. Rev. B* **102**, 155145 (2020).
- Blaž, P. et al. *WIEN2k. An Augmented Plane Wave + Local Orbitals Program for Calculating Crystal Properties* (Karlheinz Schwarz, Technical Universität Wien, Vienna, 2018).
- Momma, K. & Izumi, F. Vesta 3 for three-dimensional visualization of crystal, volumetric and morphology data. *J. Appl. Crystallogr.* **44**, 1272 (2011).

## Acknowledgements

The authors would like to thank Y. Maeno, S. Yonezawa, A. Ikeda, and Y. Matsuda for their valuable discussions. This work was supported by the Kyoto University LTM Center, Grants-in-Aid for Scientific Research (Grant Nos. JP19K14657, JP19H04696, JP20H00130, JP20KK0061, JP21K18600, JP22H04933, JP22H01168, and JP23H01124) and Grant-in-Aid for JSPS Research Fellows (Grant No. JP23KJ1247) from JSPS.

## Author contributions

F.H. and K.I. designed the research. F.H., K.K., S.K., and K.I. performed NMR/NQR measurements. Y.O. and T.O. synthesized and characterization of the bulk samples. S.M., R.Y., Y.O., and T.O. performed specific heat measurements. All authors contributed to interpreting the experimental results and finalizing the manuscript.

## Competing interests

The authors declare no competing interests.

**Additional information**

**Supplementary information** The online version contains supplementary material available at <https://doi.org/10.1038/s43246-023-00381-4>.

**Correspondence** and requests for materials should be addressed to Fumiya Hori or Kenji Ishida.

**Peer review information** *Communications Materials* thanks the anonymous reviewers for their contribution to the peer review of this work. Primary Handling Editors: Alannah Hallas and Aldo Isidori. A peer review file is available.

**Reprints and permission information** is available at <http://www.nature.com/reprints>

**Publisher's note** Springer Nature remains neutral with regard to jurisdictional claims in published maps and institutional affiliations.



**Open Access** This article is licensed under a Creative Commons Attribution 4.0 International License, which permits use, sharing, adaptation, distribution and reproduction in any medium or format, as long as you give appropriate credit to the original author(s) and the source, provide a link to the Creative Commons licence, and indicate if changes were made. The images or other third party material in this article are included in the article's Creative Commons licence, unless indicated otherwise in a credit line to the material. If material is not included in the article's Creative Commons licence and your intended use is not permitted by statutory regulation or exceeds the permitted use, you will need to obtain permission directly from the copyright holder. To view a copy of this licence, visit <http://creativecommons.org/licenses/by/4.0/>.

© The Author(s) 2023